Local and global dichotomic dysfunction in resting and evoked functional connectivity precedes tauopathy

Francesca Mandino[abc], Ling Yun Yeow[a], Renzhe Bi[a], Lee Sejin[a], Han Gyu Bae[ad], Seung Hyun Baek[a], Chun-Yao Lee[a], Hasan Mohammad[a], Chai Lean Teoh[a], Jasinda H. Lee[e], Mitchell K. P. Lai[e], Sangyong Jung[a], Yu Fu[a], Malini Olivo[a], John Gigg[b], Joanes Grandjean*[af]

a Singapore Bioimaging Consortium, Agency for Science, Technology and Research, Singapore

b Faculty of Biology, Medicine and Health, The University of Manchester, Manchester, United Kingdom

c Department of Radiology and Bioimaging Sciences, Yale School of Medicine, New Haven, CT, USA

d Department of Life Sciences, Yeungnam University, Gyeongsan, Gyeongsangbuk-do 38541, South Korea

e Department of Pharmacology, Yong Loo Lin School of Medicine, National University of Singapore

f Department of Radiology and Nuclear Medicine & Donders Institute for Brain, Cognition, and Behaviour, Donders Institute, Radboud University Medical Centre

ORCID: Francesca Mandino 0000-0002-5605-0854 - Joanes Grandjean 0000-0001-8413-0491

Corresponding author

Joanes Grandjean, PhD

Department of Radiology and Nuclear Medicine & Donders Institute for Brain, Cognition, and Behaviour, Donders Institute, Radboud University Medical Centre, Nijmegen 6525 EZ, The Netherlands

Joanes.Grandjean@radboudumc.nl

Keywords: fMRI, mouse, Alzheimer's disease, optogenetics, 3xTgAD

Abstract

Functional activity alterations are one of the earliest hallmarks of Alzheimer's disease (AD), already detected prior to beta-amyloid plaque and tau-tangle accumulation. To reveal the physiological basis underpinning these changes at the onset of the pathology, we leveraged fMRI in the 3xTgAD mouse model for AD. Resting-state fMRI revealed functional connectivity loss within areas homologous to the human temporal lobe, particularly the entorhinal cortex. Optogenetic activation of the entorhinal cortex results, instead, in enhanced fMRI signal, thus denoting an increase in metabolic demand under load. This is corroborated by synaptic hyperexcitability in the highlighted projection targets, reported with electrophysiological recordings. Thus, 3xTgAD mice reveal a dichotomic behavior between resting and evoked states, resulting in a functional brain-wide reorganization with local underpinnings, which reconciles evidence from the human literature. The 3xTgAD tauopathy profile resembles that in AD patients closely, suggesting that similar pathophysiological mechanisms might underlie network dysfunction in clinical cases.

Introduction

Tauopathies are a hallmark in many neurodegenerative disorders, including Alzheimer's disease (AD)[1]. To date, clinical trials targeting later stages of AD pathology have all either failed or made symptoms worse [2]. As such, the focus is now placed on the earliest signs and predictive biomarkers for disease progression. Synaptic dysfunction is one of the earliest events taking place prior to AD [3]. This has been revealed by abnormal functional Magnetic Resonance Imaging (fMRI) patterns during tasks, or at rest, in groups at risk for AD, such as mid-life APOEε4 risk-allele carriers [4], or amyloid-positive but cognitively-healthy elderly [5], thus, confirming the need to focus on the pre-pathological stages. Despite a strong interest in these biomarkers, the underlying mechanisms supporting abnormal connectivity changes are not known. Transgenic animals bearing mutations from familial AD and tauopathies also develop several of the distributed neuronal network dysfunctions found in AD, such as in the early stages of cerebral amyloidosis [6–8]; as such, AD models may provide important mechanistic insights. To understand the physiological basis underlying resting-state fMRI (rsfMRI) dysfunction during pre-tauopathy, we used the triple-transgenic mouse model for AD (3xTgAD) [9]. 3xTgAD mice were positive for phospho-tau, a precursor for the hallmark tauopathy of neurofibrillary tangles, in the amygdala and hippocampus, at 3 and 6 months of age.

The local connectivity loss reported at the same age points was at the stem of larger neuronal network dysfunction. Furthermore, the deficits in local connectivity showed a remarkable overlap with homologous networks affected by tauopathies in humans. We then employed optogenetics in combination with fMRI (ofMRI) to examine the evoked response from photostimulation of the lateral entorhinal cortex (ENTl), a central dysfunctional node in 3xTgAD [10,11] and AD patients [12–14]. This revealed a hyperemic response in 3xTgAD relative to wild-type mice in several distal projection areas. Our observations underscore several of the physiological underpinnings behind local and distal connectivity dysfunctions commonly observed in groups at risk of developing AD and other tauopathies, thus supporting a reconciliation for the apparent discordant results put forward in early-AD subjects [4,5,15]. This study provides a trans-species neurophysiological model for early network failures, which cascade into some of the most severe neuropathologies affecting the aging population.

Results

Phosphorylated tau in ventral-amygdaloid-striatal networks precedes amyloid deposition

To determine the pathological state, brain slices from 3xTgAD and control animals aged 3, 6, and 10 months were examined for immunoreactivity to 6e10 (targeting the N-terminus of beta-amyloid, Aβ) and AT8 (targeting phospho-tau (Ser202, Thr205)). Consistent with previous description [9,16], no immunoreactivity was observed to 6e10 at 3 and 6 months of age (Supplementary Fig. 1), while AT8 binding was revealed in the amygdala at 3 months, spreading to the hippocampus at 6 and 10 months (Fig. 1d, Supplementary Fig. 2). Only at 10 months of age did 3xTgAD exhibit the immunoreactivity patterns attributable to neurofibrillary tangles (Supplementary Fig. 2c).

We confirmed these results with ELISA performed on brain tissue homogenate. Soluble $A\beta_{1\text{-}40}$ levels in 3xTgAD were of comparable magnitude (~12000/~16000 pg/mg) to that of age-matched control animals at 3 months of age; a difference of 1.7-fold in soluble $A\beta_{1\text{-}40}$ was seen between controls (~9000 pg/ml) and 3xTgAD (~16000 pg/ml) at 6 months of age. No difference was reported for insoluble $A\beta_{1\text{-}40}$ at both age points. Furthermore, 3xTgAD mice showed an increase in total tau of several orders of magnitude compared to age-matched controls at both age points, e.g., 20-fold increment at 6 months of age. We conclude that 3xTgAD mice aged 3 and 6 months represent a pre-plaque and pre-tangle stage of AD-like pathology. The 3- and 6-months age points were, therefore, examined in the remainder of this study.

The ventral-amygdaloid-striatal network is affected during tauopathy in mice and humans

To examine spontaneous fluctuations in brain activity, we recorded rsfMRI in male 3xTgAD and wild-type control mice on the same background strain (129sv/c57bl6) at 3 (N_{3xTgAD} = 19, $N_{controls}$ = 10) and 6 months of age (N_{3xTgAD} = 13, $N_{controls}$ = 10), longitudinally. The rsfMRI protocol employed here was recently compared to others in a multicenter study, which indicated elevated sensitivity and specificity for resting-state networks detected in this dataset relative to other protocols, including an awake mouse protocol [17]. One 3xTgAD mouse developed hydrocephalus, which, despite the acute condition, only marginally affected functional connectivity [18].

This animal was removed from our study following *a priori* exclusion criteria. Firstly, we examined local connectivity coherence using the Regional Homogeneity (ReHo) method [19], a sensitive indicator of local connectivity in mice [20]. 3xTgAD mice in both age groups presented a bilateral deficit in ReHo compared to controls (Fig. 1a), localized to the ventral-amygdaloid-striatal system. The latter included the ENTl ($\Delta mean_{3months}$ = -0.007 [-0.010, -0.005]; $\Delta mean_{6months}$ = -0.006 [-0.009, -0.003], Fig. 1b) within the retrohippocampal area, the nucleus accumbens (ACB; Supplementary Fig. 3a) within the ventral striatum, basolateral amygdala (BLA; Supplementary Fig. 3b) and medial prefrontal cortex (mPFC, prelimbic cortex within the mPFC reported as example in Supplementary Fig. 3c). Concurrently, 3xTgAD mice exhibited increased ReHo in somatosensory areas, such as barrel field cortex (SSp-bfd, $\Delta mean_{3months}$ = 0.122 [0.005, 0.020], $\Delta mean_{6months}$ = 0.017 [0.006, 0.035], Supplementary Fig. 3d).

Strikingly, the functional deficit hotspots, identified with the ReHo method, overlapped with homologous areas in the human brain, namely, the ventral-amygdaloid-striatal system. These areas represent an early target for tau aggregation, as consistently highlighted in a meta-analysis for the keyword 'tauopathy' through the NeuroQuery library (Fig. 1a). Thus, the 3xTgAD model, similar to other transgenic models, e.g. PSAPP, ArcAβ [6,21,22], presents functional alterations that precede extracellular Aβ and tangle deposition. The spatial distribution of these dysfunctions confers added relevance to the 3xTgAD model for the study of early emotional-memory deficits found in patients affected by mild cognitive impairment.

Importantly, deficits within the ventral-amygdaloid-striatal system are consistent with behavioral results in young 3xTgAD, where fear and emotional processes are highly affected [23]. Emotional control, regulated by the hippocampal-prefrontal-amygdaloid system, is also affected in pre-AD patients [23,24], further highlighting the trans-species relevance of our results. Moreover, not all brain areas were affected in comparable manner: the somatosensory cortex of 3xTgAD presented elevated ReHo, reminiscent of previous findings in APP transgenic model [25]. This highlights that pathophysiology does not affect each brain region equally.

Fig. 1: Loss of functional connectivity at rest, and enhanced evoked response, in 3xTgAD.

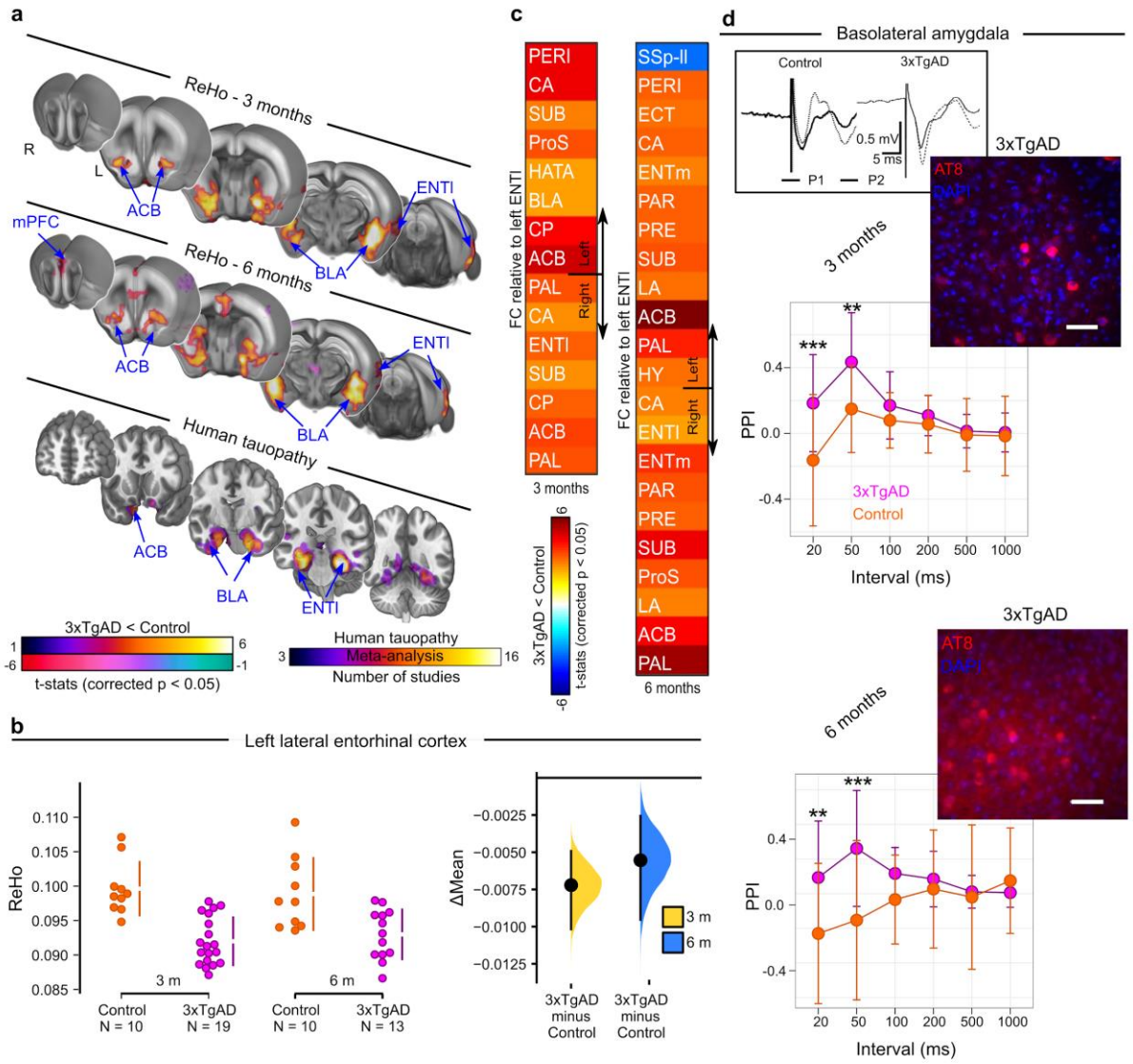

a) Regional Homogeneity (ReHo) thresholded group analysis for 3- and 6-month-old mice (top, middle) compared to human tauopathy meta-analysis (bottom). Significant decrease in ReHo within the ENTl, ACB, and BLA in 3- and 6-month-old 3xTgAD, respectively. **b)** ReHo distribution in the ENTl (left hemisphere: $\Delta mean_{3months}$ = -0.007 [-0.010, -0.005]; $\Delta mean_{6months}$ = -0.006 [-0.009, -0.003]). **c)** Pair-wise ROI interactions relative to the left ENTl: decrease of functional connectivity in contralateral ENTl, ACB, BLA at both ages. Increased functional connectivity in somatosensory regions. **d)** Paired-pulse electrical stimulation of the ENTl is recorded as fEPSPs in the BLA: increased facilitation in 3xTgAD, at both ages. Response to ENTl stimulus pairs calculated as the paired-pulse index (PPI) was reported for intervals of 20, 50, 100, 200, 500 and 1000 ms. * $p < 0.05$, ** $p < 0.005$, ***$p < 0.001$ (3 months old: $N_{controls}$ = 7, N_{3xTgAD} = 6; 6 months old: $N_{controls}$ = 4, N_{3xTgAD} = 4). Immunohistochemistry (AT8/DAPI) reveals phosphorylated tau in the BLA, at both ages (age-matched insets). Top-left inset: example of raw data for control and 3xTgAD in BLA for pulse 1 (P1) and pulse 2 (P2) at 3 months. SSp-II: somatosensory area, lower limb; ENTl: lateral entorhinal cortex; BLA: basolateral amygdala; ACB: nucleus accumbens; fEPSP: field excitatory postsynaptic potential. Scale bar: 100 µm.

Dopamine response genes are enriched in functionally compromised regions in 3xTgAD

We hypothesized that the patterns of functional alteration were the consequence of 3xTgAD transgene products interacting with others from the brain transcriptome. To test this, we searched for gene expression patterns overlapping with the functional deficits highlighted above (Fig. 1). The expression profile from 4117 genes selected for their brain expression was spatially correlated with the ReHo deficits in the 3-month-old 3xTgAD dataset (Supplementary Fig. 4). We compared the occurrence in biological processes in a ranked-test in the GOrilla database. Genes associated with dopamine signaling overlapped with regional deficits (Table 1, p-value$_{FDR}$ < 0.001). These included genes encoding for G protein signaling (Rgs9, EntrezID = 19739, r = 0.178), G protein subunit (Gnal, EntrezID = 14680, r = 0.215), and Adenylate cyclases (Adcy5, EntrezID=224129, r = 0.184, Adcy6, EntrezID = 11512, r = 0.142).

Table 1: Dopamine receptor signaling pathway genes overlap with the ReHo functional deficit in 3xTgAD

GO term	Description	p-value	FDR q-value	Enrichment
GO:0007212	dopamine receptor signaling pathway	6.8E-9	7.62E-5	16.47
Top ranking genes				
Rgs9 - regulator of g-protein signaling 9 Adcy5 - adenylate cyclase 5 Gnal - guanine nucleotide binding protein, alpha stimulating, olfactory type Gnao1 - guanine nucleotide binding protein, alpha o Drd3 - dopamine receptor d3 Drd2 - dopamine receptor d2 Drd1a - dopamine receptor d1a Adcy6 - adenylate cyclase 6				

Changes in dopamine signaling were reported previously in an animal model of cerebral amyloidosis also overexpressing APP$_{swe}$. In addition, loss of midbrain dopamine (DA) neurons, as well as deficits in hippocampus-to-ACB signaling mediated by DA, has been observed at 3 months of age in Tg2576 mice [26,27]. In AD, alterations in DA levels or DAergic receptors are found to significantly impact synaptic plasticity and hippocampal-memory encoding [28]. Loss of DA receptors, especially D2, has

been shown in areas such as the hippocampus, prefrontal cortices and BLA [29,30] in AD patients. PET studies on AD patients also confirm a loss of striatal D2-like receptors [31]. Our results, therefore, bring supporting evidence for an interaction between the DAergic system associated with early cerebral amyloidosis and tauopathy, which leads to synaptic dysfunction.

Local functional connectivity deficits translate into whole-brain network alterations

The ENTl and associated hippocampal areas are fundamental for declarative memory encoding and retrieval [32,33]. Particularly, the ENTl is among the first hubs affected in both human AD [34] and the 3xTgAD model of cerebral amyloidosis and tauopathy [9] (Fig. 1a). As such, the ENTl was targeted for further analysis. To examine distal functional connectivity alterations at rest, we assessed pair-wise ROI interactions relative to the left-hemisphere ENTl. Functional connectivity to the ENTl was decreased in the retrohippocampal and hippocampal regions (Fig. 1c, and e.g. ENTl right hemisphere: $\Delta mean_{3months}$ = -0.114 [-0.193, -0.035], $\Delta mean_{6months}$ = -0.127 [-0.205, -0.058], Supplementary Fig. 5a), ventral striatum (ACB, Supplementary Fig. 5b), and amygdala (BLA, Supplementary Fig. 5c). Similarly, an increase in functional connectivity relative to the ENTl was reported in the somatosensory cortex (lower limb, SSp-ll; Supplementary Fig. 5d). These results, focusing on the ENTl-specific network, show similarities to the whole-brain functional connectivity changes assessed with ReHo, presented in an overlapped design in Supplementary Fig. 6.

To confirm the connectivity results, we performed electrophysiological recordings in urethane-anesthetized 3xTgAD and control mice, *in vivo,* at 3 or 6 months of age. Field excitatory postsynaptic potentials (fEPSP) were assessed within the BLA and dentate gyrus (DG), following electrical stimulation in the ENTl. Paired-pulse stimulation (PPS) protocol, used to assess short-term synaptic plasticity changes, was analyzed through the paired-pulse index (PPI) and revealed a quadruple effect between ROI, age, genotype, and paired-pulse intervals: $F_{(51,46)} = 28.135$, $p < 0.001$. Specifically, no difference between 3xTgAD and controls was found for longer paired-pulse intervals in both the BLA and DG at both age points. A strong increase in facilitation was instead reported for short intervals in both BLA (e.g. 3 months old: 20 ms, z-score = -3.96, $p < 0.001$; 50 ms, z-score = -3.11, $p < 0.05$; Fig. 1d) and DG (e.g. 3 months old: 20 ms, z-score = -3.16, $p < 0.01$; 50 ms, z-score = -4.54, $p < 0.001$;

Supplementary Fig. 7). We interpreted this as indicative of neuronal synaptic hyperexcitability in 3xTgAD: intracellular Ca^{2+} residuals from the first stimulus (P1) likely elicit augmented release of the presynaptic neurotransmitter in response to the second pulse (P2). This hyperexcitable neuronal profile may, thus, support the network dysfunction observed, through compensatory mechanisms in response to the compromised functional connectivity reported at rest. Additionally, the Input/Output curve (IOC) analysis for synaptic strength revealed a quadruple interaction effect between ROIs, age, genotype, and stimulation amplitude: $F_{(35,32)} = 108.31$, $p < 0.001$. Within the BLA, 3xTgAD mice did not show significant differences compared to controls at 3 months, whereas, there was a significantly larger response at 6 months for all stimulus intensities, e.g. 300 µA ($z = -6.23$, $p < 0.001$), 450 µA ($z = -6.64$, $p < 0.001$) and 600 µA ($z = -7.1$, $p < 0.001$; Supplementary Fig. 8a). Within DG, 3xTgAD mice showed larger responses than controls by 3 months (e.g. 300 µA z-score = 2.36, $p < 0.05$ and 600 µA z-score = 2.93, $p < 0.005$; Supplementary Fig. 8b, left panel). At 6 months, there was a significant difference between genotypes for the strongest current stimulus (600 µA, z-score = 2.12, $p < 0.05$), although there was a trend for increased facilitation in 3xTgAD mice compared to controls (Supplementary Fig. 8b, right panel). Taken together, our electrophysiological evidence, assessed *in vivo*, reveals a hyperexcitable behavior during the evoked neuronal response in disease-relevant 3xTgAD brain regions, suggesting a dichotomous relationship between increased-evoked and reduced-spontaneous activity in AD-like vulnerable areas, where functional connectivity is highly compromised at rest. In an exploratory analysis, we examined whole-brain network deficits in 3xTgAD mice at 3 and 6 months of age (Supplementary Fig. 9a). Alterations were consistent between both age groups, localized within and between regions highlighted in the ReHo analysis, namely, in the amygdaloid/cerebral nuclei (including BLA and ACB), the ENTl and the hippocampal formation (Fig. 1a, Supplementary Fig. 9b). Importantly, the nodal degree distribution, i.e., the number of affected connections per ROI, was found to overlap with ReHo (Supplementary Fig. 9b). This indicates that local functional connectivity deficits translate into distal functional connectivity deficits and, in turn, greater network dysfunction. Moreover, regions highlighted in the pair-wise correlation analysis were also found to be enriched in tau aggregates within the AD-like disease progression

(amygdala and hippocampus, Supplementary Fig. 2), consistent with tau dispersions across functionally connected networks [35].

Functional connectome of the ENTl revealed by optogenetics

The ENTl is revealed above to be a major hub region affected in the 3xTgAD brain at rest. To explore its functional connectome, we leveraged fMRI combined with optogenetics (ofMRI; Fig. 2) [36] to visualize the hemodynamic response to a 10-block design photostimulation of ChR2-transfected CaMKIIα-positive (AAV5-CamKIIα-hChR2 (H134R)-mCherry) ENTl neurons ($N_{controls}$ = 10, N_{3xTgAD} =12; Fig. 2a, Supplementary Fig. 10ab). Anatomical imaging of the fiber revealed that the ENTl was accurately targeted (Fig. 2c, Supplementary Fig. 10c). Transfection led to robust expression at the target site (Fig. 2b, Supplementary Fig. 11a). Cell bodies of transfected neurons were consistent with those of excitatory pyramidal cells (Supplementary Fig. 11b). ENTl neurons faithfully responded to 5 and 20 Hz light pulse trains in both controls and 3xTgAD (Fig. 2d, Supplementary Fig. 11c). Prolonged photostimulation (500 ms) applied to patched neurons *in vitro* confirmed an effective ChR2-induced inward current on both control and 3xTgAD mice *post hoc* (Supplementary Fig. 11d). There was no evidence of aberrant spontaneous behavior to photostimulation protocols in freely behaving mice, unlike seizures previously reported following photostimulation of the hippocampus in rats [37]. An unbiased voxel-wise analysis revealed the BOLD signal associated with our modeled response in controls and 3xTgAD at 3 months of age (Fig. 2e, top and middle rows respectively) in several regions, including the hippocampal formation (hippocampus and retro hippocampal areas), the amygdaloid area (e.g. BLA), the ventral striatum (ACB), the prefrontal and the insular areas. Similar results were reported for the 6-month age point (Supplementary Fig. 12, left and middle panel). Interestingly, optogenetically-evoked activity was mostly confined to the ipsilateral hemisphere, despite the presence of contralateral projections, as predicted by viral tracers (Fig. 2e bottom row, spatial correlation r = 0.36). This supports the notion of a neuronal mechanism that silences the response contralaterally but not ipsilaterally to artificially generated neuronal activity, perhaps via feed-forward active inhibition [38].

Fig. 2: Optogenetic modulation of the lateral entorhinal cortex.

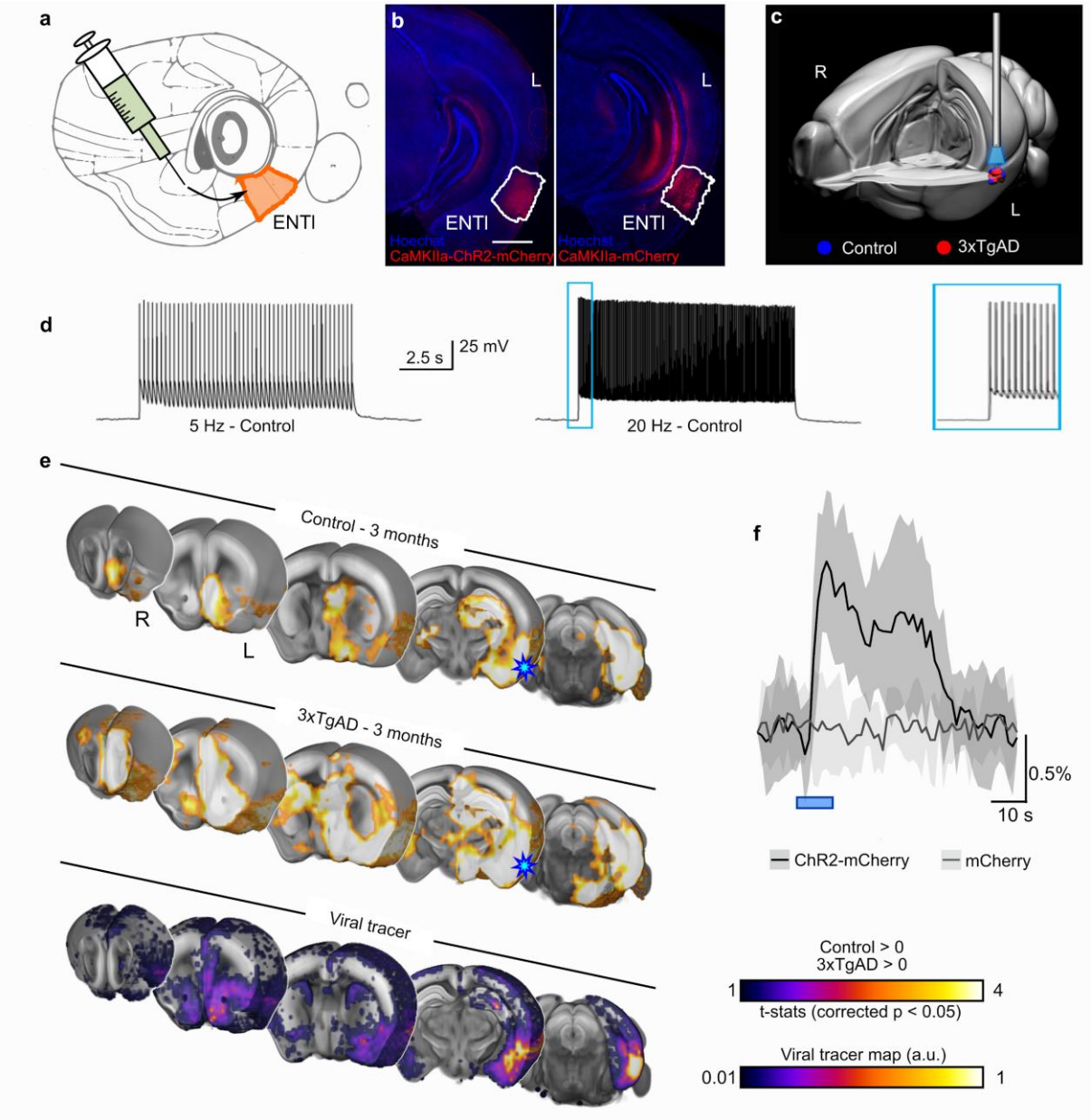

a) Diagram of stereotaxic injection in the left ENTl (in mm from Bregma and middle line: AP: -2.8, ML: +4.2, DV: -2.6). **b)** ChR2-mCherry/Hoechst (left) and mCherry/Hoechst (right) indicate successful targeting of the ENTl and stable transfection. **c)** 3-d rendering of fiber tip position for each experimental animal, red dots indicate 3xTgAD subjects (N = 12) and blue dots indicate controls (N = 10). **d)** Optogenetic stimulation of ChR2-transfected neurons at 5 Hz and 20 Hz *in vitro* shows frequency-locked spiking activity. **e)** Optogenetically-locked BOLD response overlaps with density projection maps. Top and middle sections indicating one-sample t-test for stimulation-locked BOLD response in the control group and 3xTgAD mice (N = 10, N = 12, respectively; $p < 0.05$ corrected) highlighting activation in key regions related to ENTl projections, i.e., HIP, BLA, ACB and mPFC; AIBS tracer projection density map with injection in ENTl (experiment ID: #114472145; bottom section). Stimulation site (ENTl) indicated with a blue star. **f)** BOLD response profile, averaged across 10 blocks, following 20 Hz stimulation in control mice injected with ChR2-mCherry (N = 10) and control mice injected with mCherry only (N = 9) shows an opsin-dependent BOLD response. AP: anterior-posterior; ML: medio-lateral; DV: dorso-ventral; HIP: hippocampus; BLA: basolateral amygdala; ACB: nucleus accumbens; mPFC: medial prefrontal cortex. Scale bar: 1000 μm.

The response elicited through photostimulation of ENTl was comparable between mice at 3 and 6 months of age, indicating a stable expression allowing for longitudinal analysis. A negative control carried out in healthy wild-type mice ($N_{mCherry\text{-}controls}$ = 9) transfected with mCherry alone (Fig. 2b) did not reveal the presence of a light response, except for a visual-associated response of the lateral geniculate nucleus and superior colliculus, probably due to the fiber illumination received as direct visual response to retinal illumination (Supplementary Fig. 10d). Hence, we concluded that the response recorded with ofMRI was not associated with potential heating and/or vascular photoreactivity artifacts. Photostimulation at frequencies ranging from 5 to 20 Hz indicated spatially overlapping results (Supplementary Fig. 10e), in contrast to previous research [39]. In fact, the non-specific, visually-associated response amplitude was stronger at lower frequencies (Supplementary Fig. 10d, upper panel), while the opsin-associated response was more marked at 20 Hz (Fig. 2e, Supplementary Fig. 12). The areas associated with a visual response elicited with 5 Hz stimulation were subsequently masked from our results and the remainder of the analysis focused on the 20 Hz paradigm (Supplementary Fig. 10d, lower panel).

Potentiated hemodynamic response and neuronal activity in 3xTgAD

To assess response differences across the brain, a non-parametric second-level analysis comparing the amplitude of activation between 3xTgAD and controls was carried out (Fig. 3, central segment). Group size at 6 months of age was reduced due to group attrition, e.g., detachment of the implant. Therefore, group sizes differed between 3 months ($N_{controls}$ = 10, N_{3xTgAD} = 12) and 6 months (Ncontrols = 8, N_{3xTgAD} = 10) of age. At 3 months, 3xTgAD mice showed significantly larger responses across several regions compared to controls, including the ipsilateral dorsal hippocampus, ACB, mPFC, cingulate and retrosplenial areas, and contralateral ENTl. The presence of an effect at 6 months could not be detected, potentially due to the reduced group size, or to a normalization of the response at a later age.

To examine local response amplitude, contrast of parameter estimates (COPEs) were extracted from ROIs highlighted in the voxel-wise comparison: ENTl ($\Delta mean_{3months}$ = 0.044, [0.022, 0.070]), ACB

($\Delta mean_{3months}$ = 0.15 [0.0106, 0.298]), mPFC (Fig. 3c, $\Delta mean_{3months}$ = 0.283 [0.161, 0.431]) and DG (Fig. 3f). Similar results were present at lower stimulation frequencies, although the more distal regions had a mitigated effect at lower frequencies (example for 10 Hz, controls ENTl: $\Delta mean_{3months}$ = 0.008, [-0.08, 0.09]). Data acquired at rest, prior to optogenetic stimulation, indicated ReHo deficits converging with that acquired in the previous dataset, replicating our observations above, despite lower acquisition quality due to a room temperature receiver coil instead of a cryoprobe coil (Supplementary Fig. 13).

Fig. 3: Increased optogenetically-locked response in 3xTgAD compared to controls at 3 months of age.

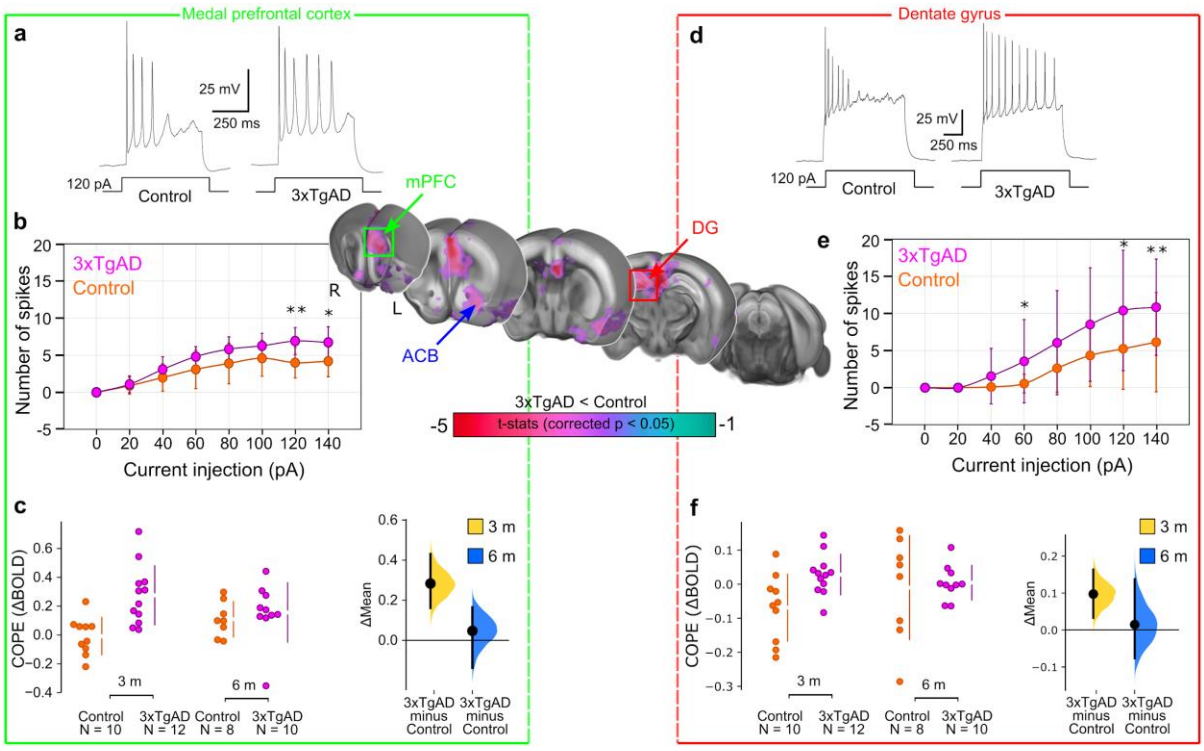

Central panel: Two-sample t-test showing significantly higher response ($p < 0.05$, corrected) in 3xTgAD compared to controls in AD-like vulnerable regions, such as mPFC and DG, left and right sections respectively. **a,d)** Representative action potential firing patterns to 120 pA injection in ILA pyramidal cells ($N_{controls}$ = 4, n = 10 / N_{3xTgAD} = 4, n = 11) and DG granule cells ($N_{controls}$ = 4, n = 29 / N_{3xTgAD} = 5, n = 18) respectively. **b, e)** The evoked spike number during various injected currents in ILA pyramidal cells and DG granule cells, respectively. The data are plotted as mean action potential numbers ± 1 SD. The statistical significance is presented with asterisks (*$p < 0.05$, **$p < 0.01$ by Mann-Whitney U test). **c, f)** COPEs are represented for 3xTgAD and controls at both age points for mPFC and DG, respectively.

To confirm the ofMRI results, we examined neuronal excitability *ex vivo* in two projection areas highlighted above, namely, the hippocampus, specifically DG, and mPFC, specifically the infralimbic area (ILA). Acute brain slice electrophysiology indicated that excitatory neurons of 3xTgAD, in both ILA (Fig. 3ab) and DG (Fig. 3de), were prone to increase the number of spikes derived by current injection compared to controls, but ILA neurons showed the enhancement of afterhyperpolarization (AHP) latency and half-width of the action potential, a phenotype consistent with previous results [40] (Supplementary Table 1), while spike morphology was comparatively unaltered (Supplementary Table 2). To examine how the alterations of the ENTl functional projectome at 3 months related to a loss of functional connectivity at rest, we projected the two responses onto the same template (Supplementary Fig. 12, right panel). There, we found that several of the ROIs, presenting a decreased functional connectivity at rest, were responding with greater amplitude to optogenetically-driven neuronal activity. This was the case for regions encompassing the ventral striatum (ACB), the dorsal DG within the hippocampal formation and prefrontal regions.

We concluded, therefore, that disturbed distal connectivity at rest translated to heightened hemodynamic response to elicited neuronal activity with optogenetics, and that this response is accompanied by hyperactivity of the embedded neurons within the affected circuits.

Discussion and conclusions

Neurological disorders, including tauopathies such as AD, are one of our greatest challenges in modern medicine. The absence of disease-modifying treatment for AD represents a major loss for the millions of patients affected by the pathology worldwide. A detailed understanding of the disease mechanisms across spatial and temporal scales constitutes a translational opportunity to facilitate the drug development process. Here, we have determined that the pre-tangle stage of the 3xTgAD mouse model presents functional connectivity patterns overlapping with areas affected by tauopathy in humans. This supports the trans-species relevance of our results.

We determined that distal connectivity disturbances could be explained by local connectivity deficits. Moreover, we observed a dichotomy between resting activity, that leads to decreased connectivity, and

evoked activity that promotes increased metabolic demand and neuronal hyperexcitability. We confirmed fMRI results with electrophysiological recordings that indicated a pathological effect on signal transmission and electrical properties of neurons in vulnerable neuronal circuits. Hence, we demonstrated that fMRI connectivity deficits are rooted in a deeper physiological context. Finally, an in-silico transcriptome analysis indicated a potential association of these results with deficits in the DA system. Importantly, our results connect to two widely examined models of AD pathological progression, namely the tau seeding hypothesis [41], and a revised amyloid hypothesis [25]. Finally, we examined potential mechanisms underpinning the electrophysiological signatures. Staging the disease progression has been an important question in AD in order to understand mechanisms and to improve diagnostics [42].

We observed phospho-tau spreading from 3 to 10 months in 3xTg AD model mice and found that this was associated with long-range connectivity deficits in young model animals. This supports the notion of a tight coupling between functional connectivity and tau progression [35], supported by molecular work by others [43]. The seeding hypothesis can be further connected to other models of axonal degeneration and inflammatory response [44] and, thus, provides a coherent description of the pathophysiology process taking place in AD.

The contribution of different Aβ species (soluble oligomers, fibrils, plaques) has been the subject of an ardent discussion within the community. Here, we demonstrate functional connectivity dysfunction in the absence of amyloid plaques and detectable elevated Aβ levels, similar to previous results in other models [6,7,25] and in subjects at risk of developing AD [4,15]. These results and others contribute to the view that the traditional amyloid cascade hypothesis for AD etiopathogenesis should be updated [45]. Our results contribute to a modern re-interpretation of the cascade and reconcile contradicting results within the human literature. Decreased resting connectivity patterns translated here into an increased response to optogenetically-driven and electrically-driven neuronal activity, thus, highlighting a possible increase in neuronal excitability following stimulation and increased metabolic demands (Fig. 3, Supplementary Fig. 12 right panel).

The dichotomy of the direction of these changes in resting and evoked activity, specifically within the ENTl network, mirrors several findings in preclinical and mild AD patients. Decreased functional connectivity is found in mild AD patients at rest, in areas related to the DMN, including the hippocampal formation [46]. However, task-based fMRI studies show increased activity in memory-related areas in subjects at risk of AD but cognitively still normal (e.g. APOEε4 carriers) suggesting a possible dichotomy in network organization of the brain at rest and in engaged status [47]. Taken together, our findings, thus, seem to reconcile apparent discordant results put forward in early-AD subjects [4,5,48].

Importantly, our results also fit into modern hypotheses for the amyloid cascade. Buckner and colleagues demonstrated that network dysfunction overlapped and preceded amyloid deposition revealed with PET [49]. Bero and colleagues demonstrated in APP transgenic models that hyper-connectivity patterns at a young age correlated with amyloid plaque distribution later in life [25]. Our results support the notion that local and distal network dysfunction at rest impairs information transmission and processing. This leads to increased metabolic demand during evoked activity, which putatively leads to circuit exhaustion and further accumulation of Aβ species through increased neuronal activity [50]. It will be important to confirm this model prediction in older 3xTgAD mice.

In sum, the functional deficits found within and relative to the temporal and ventral brain areas in 3xTgAD mice recapitulate several important effects described in pre-AD subjects with functional neuroimaging. Importantly, we postulate a disruption in DAergic signaling pathways as one of the earliest features characterizing AD development. Moreover, the photostimulation of the ENTl leads to a marked increase in BOLD response in several important projection areas. The dichotomic behavior between resting and evoked functional responses, taking place during the early stages of cerebral amyloidosis and tauopathy, reveals an endophenotype in line with the human tauopathy profile. This suggests that similar pathophysiological mechanisms might be the cause of network dysfunction in clinical cases, providing an understanding of the underlying mechanisms leading to functional deficits preceding this fatal neurodegenerative disorder.

Methods

Animal permit

All procedures conducted in the UK were performed in accordance with the UK Animals (Scientific Procedures) Act 1986 and the University of Manchester Ethical Review Panel under Home Office license PPL 70/7843. All experiments performed in Singapore Bioimaging Consortium, A*STAR, Singapore, were in accordance with the ethical standards of the Institutional Animal Care and Use Committee (A*STAR Biological Resource Centre, Singapore, IACUC #171203).

In both locations, the 3xTgAD and the control colonies were maintained 'in-house' through the pairing of homozygous individuals. Mice were housed in cages of up to five, with same-sex and genotype cage-mates in a pathogen-free environment, kept at a 45-65% humidity, under a 12:12-hour light-dark cycle and room temperature, with *ad libitum* access to food and water. The detailed breakdown of animal group sizes per experiment is detailed in Table 2.

Table 2: Animal breakdown for the experimental procedures.

	3 months		6 months		10 months
	Control	3xTgAD	Control	3xTgAD	3xTgAD
RsfMRI	10▸	19▸▸	10▸	13▸▸	-
OfMRI-ChR2	10•	12••	8•	10••	-
OfMRI-mCherry	9	-	-	-	-
PPS	7	6	4	4	-
IOC	5	4	4	3	-
Slice electrophysiology			4•	5••	-
Slice optogenetics	1	1	-	-	-
Viral expression histology	1 (ChR2-mCherry) • 1 (mCherry)	1••	-	-	-
Immunohistochemistry	2	2	2	2	2
ELISA	2•	1••	2•	4••	1

RsfMRI and ofMRI experiments were conducted on different cohorts of animals. Within each cohort, longitudinal experiments between 3- and 6-months age points were performed. Subgroups of the experimental animals that previously underwent fMRI experiments, were then used for slice electrophysiology, viral expression validation, and ELISA tests. The same symbol represents animals belonging to the same cohort or a subgroup of the same cohort. Electrophysiological experiments *in vivo* were conducted on different cohorts, being this a non-recovery procedure. Immunohistochemistry stainings were performed on a separate sample of mice.

Specifically, male 3xTgAD and control mice on the same background strain (129sv/c57bl6) aged either 3-4 months (N = 6 and N = 7, respectively) or 6-7 months old (N = 4 and N = 4, respectively) were used for electrophysiological recordings *in vivo.* Additionally, male controls (total N = 29) and 3xTgAD (total N = 31) have been used for the imaging experiments. Specifically, $N_{controls}$ = 10 and N_{3xTgAD} = 19 underwent rsfMRI experiments. Additionally, $N_{controls}$ = 19 and N_{3xTgAD} = 12 mice underwent ofMRI experiments. An *a priori* power analysis was performed following results in [21] using R (power.t.test), indicating that N = 10 per group for rsfMRI is sufficient to achieve 80% power with the following parameters: delta = 14, SD = 11, two-tailed test, significance threshold = 0.05.

Imaging: Optogenetic surgery

Male 129sv/c57bl6 and 3xTgAD mice (~30 g, N = 19, N = 12 respectively) were anesthetized with a mixture of ketamine/xylazine (ketamine 75 mg/kg, xylazine 10 mg/kg). The head was shaved and cleaned with three wipes of Betadine® and ethanol (70%). Lidocaine was administered subcutaneously, *in situ* under the scalp. Each animal was kept on a warm pad to prevent hypothermia, and the head was positioned in a stereotaxic frame; protective ophthalmic gel was applied to avoid dryness. A portion of the scalp was removed to expose the skull. The distance between Bregma and Lambda was measured and compared to the standard 4.2 mm reported in the mouse brain atlas [51]. Any deviation from 4.2 mm allowed a proportional adjustment for craniotomy coordinates. Small craniotomies were performed above the left hemisphere with a drill (burr tip 0.9 mm^2) at -2.8 from bregma, +4.2 from the midline. Virus injection into ENTl was carried out through this craniotomy at -2.8 to -2.7 mm from brain surface and cannula positioning reached -2.6 mm from the surface. Coordinates were taken according to the Paxinos mouse brain atlas [51]. An injection of adeno-associated virus (AAV) was performed in the target location using a precision pump (KD Scientific Inc., Harvard Bioscience) with a 10 µl NanoFil syringe with a 33-gauge beveled needle (NF33BV-2). The AAV used [52] (AAV5-CaMKIIa-hChR2(H134R)-mCherry ($N_{controls}$ = 10, N_{3xTgAD} = 12), AAV5-CaMKIIa-mCherry ($N_{mCherry\text{-}controls}$ = 9), titer 1-8x10^{12} vg/ml), were acquired from Vector Core at the University of North Carolina (USA). A total volume of 0.75 µl of the vector was injected in each mouse at a rate of 0.15 µl/min. The injector was kept in location for 10 minutes after injection

completion to preclude backflow. After the extraction of the needle, a fiber optic cannula (diameter 200 μm, 0.39 NA, length according to the injection site, diameter 1.25 mm ceramic ferrule) was lowered to the targeted region (Laser 21 Pte Ltd, Singapore; Hangzhou Newdoon Technology Co. Ltd, China). The cannula was fixed in place with dental cement (Meliodent rapid repair, Kulzer). Buprenorphine was administered post-surgically to each animal. Animal recovery took place on a warm pad.

Imaging: Animal preparation

Animal preparation followed a previously established protocol [53]. Anesthesia was induced with 4% isoflurane; subsequently, the animals were endotracheally intubated, placed on an MRI-compatible cradle and artificially ventilated (90 breaths/minute; Kent Scientific Corporation, Torrington, Connecticut, USA). A bolus with a mixture of Medetomidine (Dormitor, Elanco, Greenfield, Indiana, USA) and Pancuronium Bromide (muscle relaxant, Sigma-Aldrich Pte Ltd, Singapore) was administered subcutaneously (0.05 mg/kg), followed by a maintenance infusion (0.1 mg/kg/hr) administered 5 minutes later while isoflurane was simultaneously reduced and kept to 0.5%. Functional MRI was acquired 20 min following maintenance infusion onset to allow for the animal state to stabilize. Care was taken to maintain the temperature of the animals at 37 °C.

Imaging: Data acquisition and stimulation protocols

Data were acquired on an 11.75 T (Bruker BioSpin MRI, Ettlingen, Germany) equipped with a BGA-S gradient system, a 72 mm linear volume resonator coil for transmission. A 2×2 phased-array cryogenic surface receiver coil was adopted for the rsfMRI experiment (N = 29) and a 10 mm single-loop surface coil for ofMRI experiments (N = 31). Images were acquired using Paravision 6.0.1 software.
For the rsfMRI data acquisition, an anatomical reference scan was acquired using a spin-echo turboRARE sequence: field of view (FOV) = 17×9 mm^2, FOV saturation slice masking non-brain regions, number of slices = 28, slice thickness = 0.35, slice gap = 0.05 mm, matrix dimension (MD) = 200×100, repetition time (TR) = 2750 ms, echo time (TE) = 30 ms, RARE factor = 8, number of averages = 2. Functional scans were acquired using a gradient-echo echo-planar imaging (EPI)

sequence with the same geometry as the anatomical: MD = 90×60, TR = 1000 ms, TE = 15 ms, flip angle = 50°, volumes = 600, bandwidth = 250 kHz.

Parameters for the ofMRI data acquisition were adapted to the lower sensitivity of the room temperature receiver coil. The anatomical reference scan was acquired using FOV = 20×10 mm^2, number of slices = 34, slice thickness = 0.35, slice gap = 0 mm, MD = 200 × 100, TR = 2000 ms, TE = 22.5 ms, RARE factor = 8, number of averages = 2. Functional scans were acquired using FOV = 17×9 mm^2, FOV saturation slice masking non-brain regions, number of slices = 21, slice thickness = 0.45, slice gap = 0.05 mm, MD = 60 x 30, TR = 1000 ms, TE = 11.7 ms, flip angle = 50°, volumes = 720, bandwidth = 119047 Hz. Field inhomogeneity was corrected using MAPSHIM protocol. Light stimulation was provided through a blue light laser (473 nm, LaserCentury, Shanghai Laser & Optic Century Co., Ltd; ~12-15 mW output with continuous light at the tip of the fiber) controlled by in-house software (LabVIEW, National Instruments). After an initial 50 s of rest as a baseline, 5, 10 or 20 Hz light pulses were applied for 10 s followed by a 50 s rest period, in a 10-block design fashion. An additional 60 s of rest were recorded after the last block of stimulation (Supplementary Fig. 10a). The experimental groups (3xTgAD and wild-type mice with ChR2-mCherry) and the negative control group (wild-type mice with mCherry alone) underwent the same imaging protocol, i.e., one resting-state scan, followed by randomized 5 Hz, 10 Hz and 20 Hz evoked fMRI scans. The negative control group was imaged with the same imaging protocol as the experimental groups to exclude potential heating and/or vascular photoreactivity artifacts [54,55]. Additionally, in order to exclude abnormal behavior induced by the photostimulation protocol [37], all animals underwent the three stimulation sessions (5 Hz, 10 Hz, and 20 Hz) again while awake and freely walking in a behavior-chamber.

Imaging: fMRI analysis

Images were processed using a protocol optimized for the mouse and corrected for spikes (*3dDespike, AFNI;* [56], motion (*mcflirt, FSL;* [57], and B1 field inhomogeneity (*fast*). Automatic brain masking was carried out on the EPI using *bet*, following smoothing with a 0.3 mm^2 kernel (*susan*) and a 0.01 Hz high-pass filter (*fslmaths*). Nuisance regression was performed using FIX [8]. Separate classifiers were generated for rsfMRI and ofMRI. The EPIs were registered to the Allen Institute for Brain Science

(AIBS) reference template ccfv3 using SyN diffeomorphic image registration (*antsIntroduction.sh, ANTS* [58]).

Local connectivity was assessed with ReHo (*3dReHo*) [19,20]. Pair-wise region-of-interest (ROI) analysis was carried out with respect to ROIs defined in the AIBS atlas. Time series extracted with the atlas were cross-correlated to the time series from the ENTl using Pearson's correlation. The ofMRI response was examined using a general linear model (GLM) framework (*fsl_glm*). The stimulation paradigm and its first derivative were convolved using the default gamma function and used as regressors in the analysis, with motion parameters as covariates. Nomenclature and abbreviations for the brain regions are in accordance with https://atlas.brain-map.org/.

Human literature spatial meta-analysis was performed on the neuroquery.org platform on November, 8th 2019, using the term 'tauopathy' in the query ('https://neuroquery.org/query?text=tauopathy+'). The query returned 30 spatial maps depicting activation voxels in neuroimaging literature associated with the searched term (Fig. 1a).

Anatomical gene expression atlas comparison

The spatial expression profile for 4117 genes was obtained from the anatomical gene expression atlas database using the application programming interface from the AIBS [59]. The spatial correlation between the ReHo second-level statistical map and each of the genes was estimated using Pearson's correlation (*fslcc*). ReHo-gene correlations were ranked and tested for enrichment of biological processes using Gene Ontology enRIchment anaLysis and visuaLizAtion tool (GOrilla, http://cbl-gorilla.cs.technion.ac.il/) [60,61]. Enrichment was tested with Fisher's Exact test with FDR correction.

Electrophysiological recordings *in vivo*: anesthesia and surgical procedure

Anesthesia was induced via intraperitoneal (i.p) injection of urethane (1.5-1.7 g/kg of 30% w/v solution prepared in 0.9% saline; ethyl carbamate, Sigma, UK). An additional dose of urethane (50 µl of 10% w/v urethane solution prepared in 0.9% saline) was administered if complete areflexia was not reached after 40 minutes from the first injection. Mice were mounted and fixed in a stereotaxic frame and mouse adapter (Kopf 1430, USA) to immobilize the head prior to surgery. Body temperature was

maintained around 37 °C throughout the duration of the experiment with the use of a homoeothermic blanket (Harvard, UK) and a rectal thermistor probe placed underneath the abdomen. A midline scalp incision was made, and the skin retracted to expose the skull. After identifying Bregma and Lambda, the distance between these two landmarks was measured and compared to the standard 4.2 mm reported in the mouse brain atlas [51]. Any deviation from 4.2 mm allowed a proportional adjustment for craniotomy coordinates to improve the accuracy of the electrode placement. Craniotomies were made above the left hemisphere using a 0.9 mm drill bit (Fine Science Tools, Germany) and a high-speed handheld drill (Foredom, USA). Care was taken to maintain the craniotomy sites moist during the whole surgical procedure. Coordinates for craniotomy and electrode placement were marked onto the skull, relative to Bregma and the midline for recording in BLA (Bregma: AP -2.5 mm, ML: 2 mm) and DG (Bregma: AP -3.5 mm, ML: 2.5 mm), as well as stimulation of ENTl (Bregma: AP -2.8 mm, ML: 4.2 mm). Recording electrodes consisted of 32-contact probes, each laid out as 2 shanks of 16 electrodes that were 500 μm apart with 100 μm between recording points (A2x16-10-500-100-413, NeuroNexus Technologies, MI).

These were first lowered to target locations (BLA target was 4 mm ventral from the brain surface at a 15° angle from vertical in the coronal plane; the DG target was also 4 mm ventral to brain surface but along a vertical plane) and then used to record brain activity during different stimulation protocols. The 2 recording electrode shanks were coated in Vibrant CM-DiI (Sigma, UK) cell-labeling solution to allow post-mortem localization of their location with fluorescence microscopy. The stimulation electrode consisted of twisted, diameter 125 μm Teflon-insulated stainless steel wires (Advent RM, UK) and was inserted an initial 3 mm from the brain surface in one step and then slowly lowered further during continuous application of stimulating pulses (50 ms PPS, 300 μA, 0.2 ms duration pulses) until the expected responses in DG and BLA were seen on an oscilloscope.

Electrophysiological recordings *in vivo*: data acquisition

Data were recorded on a Recorder64 system (Plexon Inc, USA), and saved for offline analysis. Electrodes were connected to a head stage (fixed gain of x20) and then to a preamplifier for a total

gain of x500. Field excitatory postsynaptic potentials (fEPSPs) were recorded at a sampling rate of 5 or 10 kHz using a 12-bit A/D converter and then stored for offline analysis. A low pass filter (1 kHz) was applied to attenuate spiking activity. Electrical stimuli were delivered by a constant-current stimulator (DS3, Digitimer, UK), triggered by analog 5 V square wave pulses from a National Instruments PCI card (PCI-6071E). Timings and types of stimuli to be delivered were controlled through custom-written programs in LabVIEW (v8, National Instruments). Stimulus duration was fixed at 200 μs throughout each protocol. Two different protocols of stimulation were performed: Input/Output, for the Input/Output curve (IOC) analysis and PPS for the PPI analysis. In each mouse, the channel with the most distinctive response (as revealed through current source density analysis *post hoc*; see below) was selected for further analysis.

Electrophysiological recordings *in vivo*: stimulation protocols - Input/output curve

The IOC reflects the functional strength of synaptic connectivity: by applying different current intensities, it is possible to analyze how the response (Output voltage) changes as a function of input strength (Input current). The range of current intensities used here was 180, 300, 450 and 600 μA.

Electrophysiological recordings *in vivo*: stimulation protocols - Paired-pulse stimulation

To measure short-term synaptic plasticity, stimulus current was set to half-maximum of the response obtained in the BLA IOC paradigm, i.e., ~300 μA, and paired-pulses were delivered at this current with different paired-pulse intervals for 20 repetitions each. The range of intervals was 20, 50, 100, 200, 500 and 1000 ms.

Electrophysiological recordings *in vivo*: data analysis

For the IOC protocol, stimulation at each current intensity was repeated 20 times (runs), the initial slope of the fEPSP response measured for each repetition and then these 20 values were averaged. The mean response to each current step for each mouse was used to plot the IOC of response to current intensity by genotype, age, and ROI. For the PPS protocol, the slope for the initial fEPSP response on a selected channel was measured for both stimuli in each pair. For each pair, the fEPSP response to the

second stimulus (P2) was normalized to that of the first (P1) and expressed as PPI ratio (see equation 1, below), such that positive values indicate synaptic paired-pulse facilitation (PPF) and negative values synaptic PP depression (PPD).

$$PPI = (P2 - P1) / P1 \quad (1)$$

In the case of synaptic facilitation PPI > 0, whereas, PPI < 0 for synaptic depression. For both the IOC and PPS results, statistical analysis was performed using the statistical software R 3.6.1 (The R Foundation for Statistical Computing). Responses to the IOC (initial slope for P1) and PPI (ratio between P2 and P1) paradigms in BLA and DG at the two age points were analyzed separately with a linear mixed model analysis, using ROI, age, genotype, amplitude/intervals (amplitude for IOC and interval for PPS), and their mutual interactions as fixed effects and animal intercepts and run repeats as random effects using R package lme4. Interaction effects were determined using a likelihood ratio test. A *post hoc* analysis was performed after a general linear hypothesis test using contrast to determine genotype effects at each stimulation amplitude or interval. Correction for multiple comparisons was implemented during the contrast analysis using the R package multcomp [62,63]. Data are plotted as mean ± 1 standard deviation (SD).

Brain slice preparation and whole-cell current-clamp recordings in ILA and DG

After undergoing the scan at 6 months, 8 mice ($N_{controls}$ = 4, N_{3xTgAD} = 4) from the ofMRI experimental mice were used for a whole-cell patch recording in brain slices. The animals were deeply anesthetized with ketamine/xylazine (0.1 ml/kg) and cardiac perfusion was performed with ice-cold, oxygenated (95% O_2 / 5% CO_2) NMDG-HEPES solution consisting of 93 NMDG, 2.5 KCl, 1.2 NaH_2PO_4, 30 $NaHCO_3$, 20 HEPES, 25 Glucose, 5 sodium ascorbate, 2 thiourea, 3 sodium pyruvate, 10 $MgSO_4$, 0.5 $CaCl_2$ (in mM, pH 7.3-7.4, 300-310 mOsm). After perfusion, the brain was coronally sliced at 350 µm thickness using a VT-1200S vibratome (Leica, Germany) in ice-cold, oxygenated NMDG-HEPES solution. Brain slices were transferred to pre-warmed NMDG-HEPES solution and left to recover for 35 min with constant oxygenation at 37˚C. During this recovery, 250, 250, 500, 1000, and 2000 µl of 2 M NaCl solution were added at 10, 15, 20, 25, 30 min recovery time points, respectively, into 150 ml of the recovery solution. After recovery, brain slices were placed into HEPES-holding solution

consisting 92 NaCl, 2.5 KCl, 1.2 NaH_2PO_4, 30 $NaHCO_3$, 20 HEPES, 25 Glucose, 5 sodium ascorbate, 2 thiourea, 3 sodium pyruvate, 2 $MgSO_4$, 2 $CaCl_2$ (in mM, pH 7.3-7.4, 300-310 mOsm)[64] at room temperature. For recording, brain slices were transferred to a recording chamber perfused with CSF solution consisting of 124 NaCl, 2.5 KCl, 1.2 NaH_2PO_4, 24 $NaHCO_3$, 5 HEPES, 12.5 Glucose, 2 $MgSO_4$, 2 $CaCl_2$ (in mM, pH 7.3-7.4, 300-310 mOsm) at room temperature. Recording pipettes were prepared from borosilicate glass pipette using aP-1000 puller (Sutter Instrument, USA) to 4-7 MΩ resistance. Current-clamp recording was then performed in the infralimbic cortex layer 2/3 and hippocampal dentate gyrus using recording pipette filled with an internal solution consisting 130 K-gluconate, 0.1 EGTA, 1 $MgCl_2$, 10 HEPES, 5 NaCl, 11 KCl, 5 Phosphocreatine, 2 Mg-ATP, 0.3 Na-GTP (in mM, pH 7.3-7.4, 300-310 mOsm). Data were collected and recorded by Multiclamp 700A amplifier (Axon Instruments, USA), Digidata 1550B (Axon Instruments, USA), pCLAMP v10 (Molecular Devices, USA), and HEKA ECP10 USB (HEKA Elektronik, Germany), PatchMaster v2x90.2. Only data that met our criteria (leakage current, <100 pA; R-series, <30 MΩ) were used for further analysis. Neuronal intrinsic properties were analyzed using AxoGraph X with statistical analysis conducted using Prism 7.0 (GraphPad).

Whole-cell patch recording of acute brain slices

Mouse brains were rapidly removed after decapitation and placed in high sucrose ice-cold oxygenated artificial cerebrospinal fluid (ACSF) containing the following (in mM): 230 sucrose, 2.5 KCl, 10 $MgSO_4$, 0.5 $CaCl_2$, 26 $NaHCO_3$, 11 glucose, 1 kynurenic acid, pH 7.3, 95% O_2 and 5% CO_2. Coronal brain slices were cut at a thickness of 250 mm using a vibratome (VT1200S; Leica Biosystems) and immediately transferred to an incubation chamber filled with ACSF containing the following (in mM): 119 NaCl, 2.5 KCl, 1.3 $MgCl_2$, 2.5 $CaCl_2$, 1.2 NaH_2PO_4, 26 $NaHCO_3$, and 11 glucose, pH 7.3, equilibrated with 95% O_2 and 5% CO_2. Slices were allowed to recover at 32° C for 30 minutes and then maintained at room temperature. Experiments were performed at room temperature. Whole-cell patch-clamp recordings were performed on ENTl pyramidal cells expressing ChR2-mCherry and were visualized using a CCD camera and monitor. Pipettes used for recording were pulled from thin-walled borosilicate glass capillary tubes (length 75 mm, outer diameter 1.5 mm, inner diameter 1.1 mm, WPI)

using a DMZ Ziets-Puller (Zeitz). Patch pipettes (2–4 MW) were filled with internal solution containing (in mM): 105 K-gluconate, 30 KCl, 4 $MgCl_2$, 10 HEPES, 0.3 EGTA, 4 Na-ATP, 0.3 Na-GTP, and 10 Na_2-phosphocreatine (pH 7.3 with KOH; 295 mOsm), for both voltage- and current-clamp recordings. Photostimulation (460 nm) was delivered by an LED illumination system (pE-4000). Several trains of a square pulse of 20 ms duration with 5, 10, and 20 Hz, were delivered respectively under current-clamp mode (I = 0) to examine whether the neurons were able to follow high-frequency photostimulation. After different frequencies of photostimulation were completed, neurons were shifted to voltage-clamp mode (at -60 mV), and a prolonged square pulse of 500 ms duration was delivered, to further confirm whether ChR2-induced current could be seen in the recorded neurons. The access resistance, membrane resistance, and membrane capacitance were consistently monitored during the experiment to ensure the stability and the health of the cell.

ELISA diagnostic assay

Brains were homogenized in a Tris-HCl buffer and agitated for 30 minutes before being subjected to centrifugation at 6000 g. The supernatant was used for the detection of soluble $A\beta_{40-42}$ and the pellet was re-suspended in Tris-HCl and 10 µl was used for further processing for insoluble Aβ ELISA as recommended by the ELISA kit (incubation with 5 M Guanidine to solubilize any aggregates and diluted before adding into ELISA plates). Samples were diluted only when necessary (phospho-tau and total tau were diluted 2x, no dilution for Aβ ELISAs). As readings could be affected by the sample volume in each well, we normalized the ELISA results to protein assay results of the same fraction, hence, the final units were in picogram of Aβ or tau in per milligram of protein (pg/mg protein).

Immunohistochemistry for AT8 and 6e10

Immunohistochemical analyses were performed as described previously in [65]. Brains of $N_{controls} = 6$ (2 per age point: 3, 6 and 10 months of age) and $N_{3xTgAD} = 6$ (2 per age point: 3, 6 and 10 months of age) were fixed by perfusion with 4% paraformaldehyde (PFA) in 0.01 M phosphate buffer solution (PBS) and then in PFA and 30% sucrose for 48 h at 4 °C. Fixed brains were cut on a microtome (CM3050S, Leica Microsystems, Nussloch, Germany) into 45 µm-thick sections and collected into a cold

cryoprotectant solution (80 mM K2HPO4, 20 mM KH2PO4, 154 mM NaCl, 0.3 g/ml sucrose, 0.01 g/ml polyvinylpyrrolidone, 30% vol/vol ethylene glycol). Sections were washed 5 times for 3 minutes in 1 x PBS and blocked in 5% FBS with 0.1% Triton X-100 for 1 hour, followed by overnight incubation with the primary antibody in blocking solution at 4 °C. These brain sections were then immunostained with primary antibodies against Aβ (6E10, Covance Research Products Inc Cat #SIG-39300-1000 RRID: AB_10175637) and phospho-tau (AT8 ThermoFisher Scientific, Cat. #MN1020). After the primary antibody binding step sections were washed 5 times in 1 x PBS for 3 min and then incubated with anti-mouse Alexa 488 or anti-rabbit Alexa 594 for 2 hours followed by washing 3 times with 1 x PBS for 3 minutes. Sections were then mounted with DAPI plus mounting media on slides. All pictures were taken by using a confocal microscope with a 40× objective.

Ex vivo histology

After the completion of the experiments, animals were injected with an overdose of ketamine/xylazine and transcardially perfused with PBS (0.01 M) followed by 4% PFA in 0.01 M PBS. After extraction, the brain was post-fixed in 4% PFA overnight. Brain sections of 50 µm were made with a vibratome (VBT1200s, Leica) and fluorophore expression, together with Hoechst staining, was checked through a confocal microscope Ti-E; DS-Qi2; Fluorescence, SBIC-Nikon Imaging Center, Singapore) for anatomical confirmation of viral injection and fiber optic cannula positioning (Fig. 2).

Statistics and data availability

Descriptive statistics for neuroimaging data are given as mean difference and [95th confidence interval] unless stated otherwise, and graphically represented as 'Gardner–Altman plots' (https://www.estimationstats.com/; [66]). If not specified, descriptive statistics are provided for left hemisphere ROIs. The statistical threshold for significance was set at $p < 0.05$, two-tailed. Voxel-wise was carried out with a non-parametric permutation-based (5000 permutations) test (*randomize*). Cluster correction was carried out with threshold-free cluster enhancement (tfce). Thresholded t-statistic for one-sample and two-sample t-tests ($p < 0.05$, tfce corrected) are shown as a color-coded overlay on the AIBS template. ROI analysis was carried out with a linear mixed model using genotype

and age as fixed effects and individual intercepts as random effects, using the lme4 package (1.1-21) for R (https://cran.r-project.org/, 3.5.3, "Great Truth"). Significance was assessed with general linear hypothesis tests implemented in the multcomp (1.4-10) package and corrected with the false discovery rate.

Data availability

Both the rsfMRI and ofMRI datasets are made publicly available on https://openneuro.org/ (**ProjectID: Mouse_rest_3xTG, Mouse_opto_3xTG**).

Acknowledgments

This work was supported by the Singapore BioImaging Consortium core funding, Singapore BioImaging Consortium award #2017 to FM and #2016 to JGr. FM was supported by a Ph.D. scholarship funded through the A*STAR Research Attachment Programme and the University of Manchester (awarded to JGi). This work was also supported by the A*STAR Investigatorship (awarded to FY) and JCO grant (BMSI/15-800003-SBIC-OOE) awarded to SY.

CRediT authors contribution

FM: Conceptualization, Formal analysis, Investigation, Methodology, Validation, Visualization, Writing - original draft, Writing - review and editing, Funding acquisition.

LYY, RB, LS, HGB, SHB, CYL, HM, CLT, JHL: Validation, Writing - Review & Editing

RB: Software, Methodology, Writing - Review & editing.

FY, SY, MKPL: Validation, Resources, Writing - Review & Editing, Funding acquisition.

MO: Resources, Writing - Review & Editing, Supervision, Funding acquisition.

JGi: Conceptualization, Resources, Writing - Review & Editing, Supervision, Funding acquisition.

JGr: Conceptualization, Methodology, Formal analysis, Data curation, Software, Resources, Writing - Review & Editing, Supervision, Funding acquisition.

Conflicts of interests

The authors have no conflict of interest to disclose.

References

1. Ballatore, C., Lee, V. M.-Y. & Trojanowski, J. Q. Tau-mediated neurodegeneration in Alzheimer's disease and related disorders. *Nature reviews neuroscience* **8**, 663–672 (2007).
2. Aisen, P. S., Vellas, B. & Hampel, H. Moving towards early clinical trials for amyloid-targeted therapy in Alzheimer's disease. *Nature reviews. Drug discovery* **12** 324 (2013).
3. Sperling, R. A. *et al.* Toward defining the preclinical stages of Alzheimer's disease: Recommendations from the National Institute on Aging-Alzheimer's Association workgroups on diagnostic guidelines for Alzheimer's disease. *Alzheimers & dementia* **7**, 280–292 (2011).
4. Filippini, N. *et al.* Distinct patterns of brain activity in young carriers of the APOE- 4 allele. *Proceedings of the National Academy of Sciences* **106** 7209–7214 (2009).
5. Sheline, Y. I. *et al.* Amyloid plaques disrupt resting state Default Mode Network connectivity in cognitively normal elderly. *Biological psychiatry* **67** 584–587 (2010).
6. Shah, D. *et al.* Resting State fMRI reveals diminished functional connectivity in a mouse model of amyloidosis. *PLoS ONE* **8** e84241 (2013).
7. Grandjean, J. *et al.* Early alterations in functional connectivity and white matter structure in a transgenic mouse model of cerebral amyloidosis. *The journal of neuroscience* **34** 13780–13789 (2014).
8. Zerbi, V., Grandjean, J., Rudin, M. & Wenderoth, N. Mapping the mouse brain with rs-fMRI: An optimized pipeline for functional network identification. *Neuroimage* **123**, 11–21 (2015).
9. Oddo, S. *et al.* Triple-transgenic model of Alzheimer's disease with plaques and tangles: intracellular Abeta and synaptic dysfunction. *Neuron* **39**, 409–421 (2003).
10. Mastrangelo, M. A. & Bowers, W. J. Detailed immunohistochemical characterization of temporal and spatial progression of Alzheimer's disease-related pathologies in male triple-transgenic mice. *BMC neuroscience* **9**, 81 (2008).
11. Yeh, C.-Y., Vadhwana, B., Verkhratsky, A. & Rodríguez, J. J. Early astrocytic atrophy in the entorhinal cortex of a triple transgenic animal model of Alzheimer's disease. *ASN Neuro* **3**, 271–279 (2011).

12. Zuo, M. *et al.* Aberrant brain regional homogeneity and functional connectivity of entorhinal cortex in vascular mild cognitive impairment: a resting-state functional MRI study. *Frontiers in neurology* **9**, 1177 (2018).
13. Zhou, M., Zhang, F., Zhao, L., Qian, J. & Dong, C. Entorhinal cortex: a good biomarker of mild cognitive impairment and mild Alzheimer's disease. *Reviews in the neurosciences* **27**, 185–195 (2016).
14. Khan, U. A. *et al.* Molecular drivers and cortical spread of lateral entorhinal cortex dysfunction in preclinical Alzheimer's disease. *Nature neuroscience* **17** 304–311 (2014).
15. Sheline, Y. I. *et al.* APOE4 allele disrupts resting state fMRI connectivity in the absence of amyloid plaques or decreased CSF A 42. *Journal of neuroscience* **30** 17035–17040 (2010).
16. Davis, K. E., Fox, S. & Gigg, J. Increased hippocampal excitability in the 3xTgAD mouse model for Alzheimer's disease in vivo. *PLoS One* **9**, e91203 (2014).
17. Grandjean, J. *et al.* Common functional networks in the mouse brain revealed by multi-centre resting-state fMRI analysis. *Neuroimage* **205**, 116278 (2020).
18. Mandino, F., Yeow, L. Y., Gigg, J., Olivo, M. & Grandjean, J. Preserved functional networks in a hydrocephalic mouse. *Matters* (2019) doi:10.19185/matters.201905000001.
19. Zang, Y., Jiang, T., Lu, Y., He, Y. & Tian, L. Regional homogeneity approach to fMRI data analysis. *Neuroimage* **22** 394–400 (2004).
20. Wu, T. *et al.* Altered regional connectivity reflecting effects of different anaesthesia protocols in the mouse brain. *Neuroimage* **149**, 190–199 (2017).
21. Grandjean, J. *et al.* Complex interplay between brain function and structure during cerebral amyloidosis in APP transgenic mouse strains revealed by multi-parametric MRI comparison. *Neuroimage* **134**, 1–11 (2016).
22. Shah, D. *et al.* Early pathologic amyloid induces hypersynchrony of BOLD resting-state networks in transgenic mice and provides an early therapeutic window before amyloid plaque deposition. *Alzheimers & dementia* **12**, 964–976 (2016).
23. España, J. *et al.* Intraneuronal β-amyloid accumulation in the amygdala enhances fear and anxiety in Alzheimer's disease transgenic mice. *Biological psychiatry* **67**, 513–521 (2010).

24. Sturm, V. E. *et al.* Heightened emotional contagion in mild cognitive impairment and Alzheimer's disease is associated with temporal lobe *degeneration. Proceedings of the national academy of sciences USA* **110**, 9944–9949 (2013).

25. Bero, A. W. *et al.* Bidirectional relationship between functional connectivity and amyloid-β deposition in mouse brain. *Journal of neuroscience* **32**, 4334–4340 (2012).

26. Cordella, A. *et al.* Dopamine loss alters the hippocampus-nucleus accumbens synaptic transmission in the Tg2576 mouse model of Alzheimer's disease. *Neurobiology of disease* **116**, 142–154 (2018).

27. Nobili, A. *et al.* Dopamine neuronal loss contributes to memory and reward dysfunction in a model of Alzheimer's disease. *Nature communications* **8**, 1-14 (2017).

28. Koch, G. *et al.* Altered dopamine modulation of LTD-like plasticity in Alzheimer's disease patients. *Clinical neurophysiology* **122** 703–707 (2011).

29. Joyce, J. N., Kaeger, C., Ryoo, H. & Goldsmith, S. Dopamine D2 receptors in the hippocampus and amygdala in Alzheimer's disease. *Neuroscience letters* **154**, 171–174 (1993).

30. Kemppainen, N. *et al.* Hippocampal dopamine D2 receptors correlate with memory functions in Alzheimer's disease. *European journal of neuroscience* **18**, 149–154 (2003).

31. Tanaka, Y. *et al.* Decreased striatal D2 receptor density associated with severe behavioral abnormality in Alzheimer's disease. *Annals of nuclear medicine* **17**, 567–573 (2003).

32. van Strien, N. M., Cappaert, N. L. M. & Witter, M. P. The anatomy of memory: an interactive overview of the parahippocampal–hippocampal network. *Nature reviews neuroscience* **10** 272–282 (2009).

33. Buzsáki, G. & Moser, E. I. Memory, navigation and theta rhythm in the hippocampal-entorhinal system. *Nature neuroscience* **16**, 130–138 (2013).

34. Van Hoesen, G. W., Hyman, B. T. & Damasio, A. R. Entorhinal cortex pathology in Alzheimer's disease. *Hippocampus* **1**, 1–8 (1991).

35. Franzmeier, N. *et al.* Functional connectivity associated with tau levels in ageing, Alzheimer's, and small vessel disease. *Brain* **142** 1093–1107 (2019).

36. Lee, J. H. *et al.* Global and local fMRI signals driven by neurons defined optogenetically by type

and wiring. *Nature* **465**, 788–792 (2010).

37. Weitz, A. J. *et al.* Optogenetic fMRI reveals distinct, frequency-dependent networks recruited by dorsal and intermediate hippocampus stimulations. *Neuroimage* **107**, 229–241 (2015).
38. Histed, M. H. Feedforward Inhibition Allows Input Summation to Vary in Recurrent Cortical Networks. *eNeuro* **5**, (2018).
39. Chan, R. W. *et al.* Low-frequency hippocampal–cortical activity drives brain-wide resting-state functional MRI connectivity. *Proceedings of the National Academy of Sciences* **114** E6972–E6981 (2017).
40. Wang, L. *et al.* Cognitive recovery by chronic activation of the large-conductance calcium-activated potassium channel in a mouse model of Alzheimer's disease. *Neuropharmacology* **92** 8–15 (2015).
41. Holmes, B. B. *et al.* Proteopathic tau seeding predicts tauopathy in vivo. *Proceedings of the National Academy of Sciences* **111** E4376–E4385 (2014).
42. Selkoe, D., Mandelkow, E. & Holtzman, D. Deciphering Alzheimer disease. *Cold Spring Harbor perspectives in medicine* **2**, a011460 (2012).
43. Clavaguera, F. *et al.* Brain homogenates from human tauopathies induce tau inclusions in mouse brain. *Proceedings of the National Academy of Sciences* **110** 9535–9540 (2013).
44. Krstic, D. & Knuesel, I. Deciphering the mechanism underlying late-onset Alzheimer disease. *Nature reviews neurology* **9**, 25–34 (2013).
45. Hardy, J. & Higgins, G. Alzheimer's disease: the amyloid cascade hypothesis. *Science* **256** 184–185 (1992).
46. Greicius, M. D., Srivastava, G., Reiss, A. L. & Menon, V. Default-mode network activity distinguishes Alzheimer's disease from healthy aging: evidence from functional MRI. *Proceedings of the National Academy of sciences U. S. A.* **101**, 4637–4642 (2004).
47. Bookheimer, S. Y. *et al.* patterns of brain activation in people at risk for Alzheimer's disease. *New England journal of medicine* **343** 450–456 (2000).
48. Braskie, M. N. *et al.* Increased fMRI signal with age in familial Alzheimer's disease mutation carriers. *Neurobiology of aging* **33** 424.e11–424.e21 (2012).

49. Buckner, R. L. molecular, structural, and functional characterization of Alzheimer's disease: evidence for a relationship between default activity, amyloid, and memory. *Journal of neuroscience* **25** 7709–7717 (2005).

50. Bero, A. W. *et al.* Neuronal activity regulates the regional vulnerability to amyloid-β deposition. *Nature neuroscience* **14**, 750–756 (2011).

51. Paxinos, G. & Franklin, K. B. J. *The mouse brain in stereotaxic coordinates*. (Houston, Gulf Professional Publishing, 2004).

52. Deisseroth, K. Optogenetics. *Nature methods* **8**, 26–29 (2011).

53. Grandjean, J., Schroeter, A., Batata, I. & Rudin, M. Optimization of anesthesia protocol for resting-state fMRI in mice based on differential effects of anesthetics on functional connectivity patterns. *Neuroimage* **102,** 838–847 (2014).

54. Christie, I. N. *et al.* fMRI response to blue light delivery in the naïve brain: implications for combined optogenetic fMRI studies. *Neuroimage* **66**, 634–641 (2013).

55. Rungta, R. L., Osmanski, B.-F., Boido, D., Tanter, M. & Charpak, S. Light controls cerebral blood flow in naive animals. *Nature communications* **8**, 14191 (2017).

56. Cox, R. W. AFNI: software for analysis and visualization of functional magnetic resonance neuroimages. *Computers and biomedical research* **29**, 162–173 (1996).

57. Smith, S. M. *et al.* Advances in functional and structural MR image analysis and implementation as FSL. *Neuroimage* **23** S208–S219 (2004).

58. Avants, B. B., Tustison, N. & Song, G. Advanced normalization tools (ANTS). *Insight J.* **2**, 1–35 (2009).

59. Ng, L. *et al.* An anatomic gene expression atlas of the adult mouse brain. *Nature neuroscience* **12**, 356–362 (2009).

60. Eden, E., Navon, R., Steinfeld, I., Lipson, D. & Yakhini, Z. GOrilla: a tool for discovery and visualization of enriched GO terms in ranked gene lists. *BMC Bioinformatics* **10**, 48 (2009).

61. Eden, E., Lipson, D., Yogev, S. & Yakhini, Z. Discovering motifs in ranked lists of DNA sequences. *PLoS computational biology* **3**, e39 (2007).

62. Bates, D., Mächler, M., Bolker, B. & Walker, S. Fitting Linear Mixed-Effects Models Using

lme4. *Journal of statistical software* **67** (2015).

63. Bretz, F., Hothorn, T. & Westfall, P. Multiple Comparisons Using R. (2016) doi:10.1201/9781420010909.

64. Ting, J. T. et al. Preparation of acute brain slices using an optimized N-methyl-D-glucamine protective recovery method. *JoVE (Journal of Visualized Experiments)*, **132**, e53825 (2018).

65. Baek, S. H. *et al.* Inhibition of Drp1 ameliorates synaptic depression, Aβ deposition, and cognitive impairment in an Alzheimer's disease model. *The journal of neuroscience* **37** 5099–5110 (2017).

66. Ho, J., Tumkaya, T., Aryal, S., Choi, H. & Claridge-Chang, A. Moving beyond P values: data analysis with estimation graphics. *Nature methods* **16**, 565–566 (2019).